Modeling the electrocatalytic nitrate removal in a rotating cylinder electrode reactor

Roger Oriol [a], José L. Nava [b], Enric Brillas [a], Oscar M. Cornejo [a,c,**], Ignasi Sirés [a,*]

[a] Laboratori d'Electroquímica dels Materials i del Medi Ambient, Departament de Ciència de Materials i Química Física, Secció de Química Física, Facultat de Química, Universitat de Barcelona, Martí i Franquès 1-11, 08028 Barcelona, Spain
[b] Departamento de Ingeniería Geomática e Hidráulica, Universidad de Guanajuato, Av. Juárez 77, Zona Centro, 36000 Guanajuato, Guanajuato, Mexico
[c] Facultad de Ciencias Químicas, Benemérita Universidad Autónoma de Puebla, Mexico

ABSTRACT

Here, computational fluid dynamics (CFD) simulations have been employed to investigate the transport phenomena occurring in an electrochemical reactor, equipped with an AISI 1018 carbon steel rotating cylinder electrode (RCE), during nitrate electroreduction. A model that resulted from solving the fundamental transport equations that govern the hydrodynamics, mass transport, and current distribution is proposed to assess the behavior of the RCE reactor when addressing the nitrate removal. The results obtained from the simulations offered a wider understanding of the selected electroreduction process. It was determined that the six surrounding Ti|IrO$_2$-based anodes acted as deflectors that promoted the presence of two Taylor vortices, giving rise to three distinct velocity zones inside the reactor. This fact had an impact on mass transport, since the appearance of low-concentration zones was associated with a greater velocity. Furthermore, a slight current distribution ($0.990 < j_c/j_{c,AVE} < 1.005$) was observed along the RCE length due to the two Taylor vortices. The model was validated by performing a series of nitrate electroreduction experiments in an RCE reactor filled with solutions of 400 mL, corroborating that it is sufficiently robust to predict the nitrate concentration decay. At 1000 rpm, operating at 447 A m^{-2} to ensure mass transport control conditions, 90 % nitrate removal from a 10 mM KNO$_3$ + 500 mM K$_2$SO$_4$ solution was achieved in only 10 min, with a low electrochemical energy consumption of 14.3 Wh g^{-1}.

1. Introduction

Nitrate water pollution is a pressing environmental issue that threatens people and ecosystems. Although nitrates are naturally present in nature, being an absolutely essential nitrogen source for plant growth, excessive levels are known cause severe health and environmental concerns, putting at risk the future of entire populations [1–3].

Several human activities, particularly agriculture and livestock farming, are the primary source for NO$_3^-$ discharge into water bodies [4,5]. The expansive use of synthetic fertilizers and the spread of livestock manure on agricultural land eventually results in nitrate leaching or in-situ generation, thereby ending in groundwater and surface water bodies. Consequently, drinking water sources fed with such polluted streams may exceed the nitrate threshold values established by the law,

posing serious health hazards [4–7]. Furthermore, improper disposal or inadequate treatment of industrial waste adds to nitrate discharge into nearby water bodies, exacerbating the pollution problem.

The health implications of long-term water pollution by NO$_3^-$ are subject to discussion, although there is consensus on the worrisome consequences derived from its presence in freshwater and drinking water, particularly for vulnerable people such as infants and pregnant women [7]. Once ingested, nitrates can be converted into nitrites within the body, which bind to hemoglobin in the blood reducing the oxygen transport efficiency [7–9]. This condition, so-called methemoglobinemia, can cause oxygen depletion, leading to severe health complications and, in some extreme cases, death.

These concerns bring about the urgent need to address NO$_3^-$ removal from water. A set of methods has been developed for this purpose so far,

including chemical and biological approaches, but electrochemical approaches have gradually gained attention among the former due to their effectiveness, cost-efficiency, simple operation and environmental compatibility [2,10–13]. Since nitrate electroreduction is a surface phenomenon, its removal is highly affected by the cathode composition and surface area. Several cathode materials have been tested, including carbonaceous materials, metal oxides, and composite electrodes [13]. Cheap materials with sufficient stability and high electrocatalytic activity are often preferred. In addition, the applied cathodic potential (E_{cath}) or cathodic current density (j_c), and solution pH have impact on the process mechanism, which can be either direct or indirect [14,15]. In dilute NO_3^- solutions (<1 M) at neat-neutral or alkaline pH, the direct path is favored because the absorbed NO_3^- is reduced by the electrons supplied at the cathode surface. Conversely, in the indirect path, NO_3^- reacts with adsorbed atomic hydrogen, an intermediate of hydrogen evolution reaction (HER) (1), yielding the absorbed NO_2^- species according to reaction (2), which is known to be the rate-determining step of the overall electrochemical nitrate electroreduction process [14–16]. Afterward, further reduction of NO_2^- on the cathode surface yields NH_3 or N_2 via reactions (3) and (4), respectively. The electrochemical nitrate reduction has been widely studied in recent years, showing outstanding results regarding the removal percentage and the possibility of accumulating less hazardous products or even valorizing them [16–21].

$$2H_2O + 2e^- \rightarrow H_2 + 2OH^- \tag{1}$$

$$NO_3^- + H_2O + 2e^- \rightarrow NO_2^- + 2OH^- \tag{2}$$

$$NO_2^- + 5H_2O + 6e^- \rightarrow NH_3 + 7OH^- \tag{3}$$

$$2NO_2^- + 4H_2O + 6e^- \rightarrow N_2 + 8OH^- \tag{4}$$

A critical element to consider in the NO_3^- electroreduction is the cell configuration, which significantly affects the efficiency of the process, since the electrode arrangement as well as the flow pattern or hydrodynamics affect the mass transport and the current distribution inside the cell [18,22,23]. In this context, the rotating cylinder electrode (RCE) reactor has been suggested as a viable system to promote the fast and complete electroreduction of NO_3^- [24,25]. More specifically, González Pérez and Bisang [24] carried out potentiostatic experiments using a reactor equipped with an RCE made of Cu (38-mm diameter and 100-mm length) to treat 900 mL of a 30 mM NO_3^- + 0.1 M K_2SO_4 solution at pH 5.6. In that work, a nitrate conversion greater than 80 % with a high selectivity towards ammonia was achieved after 1 h at $E_{cath} = -1.3$ V vs SCE and 1000 rpm. On the other hand, Oriol et al. [25] performed the treatment of 400 mL of a 10 mM NO_3^- + 0.05 M Na_2SO_4 solution at pH 6.5 using a batch system equipped with an AISI 1018 carbon steel RCE (38-mm diameter). The complete removal of nitrate was attained after 120 min at $E_{cath} = -1.8$ V vs mercurous sulfate reference electrode (MSE) and 500 rpm. Those works show the outstanding performance of the RCE reactor for nitrate reduction. The RCE reactor has been widely used in electrochemical engineering, being especially noticeable its use in metal recovery [26–28]. The mass transport is dramatically enhanced by the central RCE rotation, upgrading the supply of electroactive species to the electrode, which results in high reaction rates and current efficiencies [26–30]. The latter can be explained by the fact that turbulence is reached at low rotation rates, corresponding to a critical *Re* value ranging from 50 to 300 for an RCE with a smooth surface [27,31].

Despite the well-known experimental and simulated functioning of the RCE reactor, it is essential to transfer this understanding to the complex phenomena that occur in nitrate electroreduction. In this regard, computational fluid dynamics (CFD) tools have arisen as an efficient strategy to elucidate the hydrodynamics, mass transport, and potential-current distribution inside different electrochemical reactors [22,23,32–36]. By solving the conservation equations linked to each phenomenon, which considers the deviation of the fluid ideality by CFD, a more intricate and insightful comprehension of the overall performance of the reactor can be attained [23].

Within the water treatment field, CFD models have been used to characterize several electrochemical reactor configurations, achieving results able to replicate the actual reactor performance [32–36]. For instance, CFD techniques have been employed to elucidate the hydrodynamic behavior of parallel plates [33,37–41], serpentine arrays [33], stacked cells [42,43] and RCE reactors [35,36,44,45]. These studies allow a deeper understanding of the dynamics of the fluid elements, thereby easing the elucidation of the influence of the flow rate and the reactor geometry on the velocity inside the reactor. The hydrodynamic models are often validated through residence time distribution (RTD) curves that quantitively describe the deviation of the fluid from the ideality, being feasible to evaluate the agreement with an ideal behavior [33,37–43]. Moreover, the conservation equations that describe the mass transport as well as the potential and current distribution can be coupled to the hydrodynamic model to obtain a complete description of the reactor in terms of yield of products and current distribution [22,23]. By simultaneously solving the mass transport and potential distribution equations, several electrochemical processes such as the active chlorine electrosynthesis [34,46], electrodissolution of metals in the electrocoagulation process [35,43,47] and metal electrodeposition [36,44,48] have been correctly described and validated. It can then be concluded that CFD techniques are powerful tools to accurately describe a wide variety of electrochemical processes. Nonetheless, most of the works were focused on metal recovery, electrosynthesis and electrocoagulation, which leaves a gap related to nitrate removal. To solve the conservation equations proposed for each model, the most common software packages employed are COMSOL® Multuyphisics and OpenFOAM.

Most of the published works dealing with nitrate electroreduction focused on assessing the performance of different cathode materials or optimizing the operation parameters to improve the process efficiency [14,15,18–20]. Nonetheless, to the authors knowledge, the mathematical model and CFD tools that describe the RCE reactor have not yet been applied to study the nitrate electroreduction.

In this article, a CFD model has been developed to simulate the hydrodynamic pattern, mass transport phenomena, and current distribution within an RCE reactor applied to nitrate electroreduction. The transport equations of momentum, mass, and charge (under turbulent flow conditions) were solved by the finite element method using a commercial code. The CFD model was used to validate the influence of peripheral velocity and NO_3^- initial concentration on the pollutant removal rate in a 400-mL RCE reactor. Through this modeling study, it is expected that a better understanding of electrochemical nitrate removal mechanisms is attained, thereby inspiring new ways to optimize the performance. The main products generated during nitrate reduction have been quantified as well.

2. Experimental

2.1. Chemicals

The solutions used in this work were prepared with analytical grade electrolytes, including KNO_3 (98 %) and K_2SO_4 (99.9 %) provided by Panreac. Phthalic acid (99.5 %) and tris(hydroxymethyl)aminomethane (99.8 %) used to prepare the mobile phase for nitrate quantification by ion chromatography were of analytical grade from Panreac. Analytical grade sodium nitroprusside dihydrate from Merck, phenol (>99 %) from Sigma-Aldrich, and EDTA (>99 %) from Panreac were used for the ammonia colorimetric determination. All solutions employed in this work were prepared with ultrapure water (Millipore Milli-Q system with $\rho > 18.2$ MΩ cm at room temperature).

Table 1
Peripheral velocities, Reynolds numbers and limiting current densities (calculated through Eq. (6)) for each rotation rate.

ω/rpm	U/cm s^{-1}	*Re*	j_L/A m^{-2}
300	59.7	25,775	257
400	79.6	34,367	293
600	119.4	51,550	353
800	159.2	68,733	403
1000	198.9	85,873	447

2.2. Experimental setup

The RCE reactor consisted of a jacketed glass vessel (13.0 cm height × 8.0 cm diameter). It comprised an AISI 1018 carbon steel RCE (14.0 cm height × 3.8 cm diameter) placed in the center of the vessel and surrounded by six commercial Ti|IrO$_2$-based anode plates (15.0 cm height × 2.0 cm wide) from NMT Electrodes. These plates were fixed in a polylactic acid plastic holder, whereas the cathode was insulated at the bottom by means of a polypropylene cap. The gap between the cathode and each anode was kept at 1.9 cm, being the total cathode and anode area exposed to the solution similar in all trials (~100 cm^2 each). The reproducibility of the trials was ensured by cleaning the steel RCE after each electrolysis with a 20 % H$_2$SO$_4$ solution, followed by further polishing of the surface with 280 and 800 grit sheet sandpaper. The RCE reactor was operated in batch mode. A variable rotation electric motor RW 20 from IKA allowed fixing the rotation rate of the RCE, whereas a GVD310 power supply from GRELCO provided the constant applied current. More details about the RCE reactor setup can be found elsewhere [25].

The NO$_3^-$ electroreduction was performed in the RCE reactor containing 400 mL of a 500 mM K$_2$SO$_4$ solution at natural pH (~6.5), assessing the influence of the rotation rate (ω) in the range of 300–1000 rpm, and nitrate initial concentration within 10–40 mM range. Since nitrate is a negatively charged ion, its mass transport towards the cathode to become electroreduced is expected to occur mainly by diffusion-convection, whereas migration plays a negative effect. To neglect such negative contribution during the electrolytic trials, a sufficiently high concentration of supporting electrolyte (i.e., K$_2$SO$_4$) was added. This minimized the nitrate transport number ($t_{NO_3^-}$), being much lower than that of SO$_4^{2-}$. This was determined from $t_{NO_3^-} = \frac{\lambda_{NO_3^-} C_{NO_3^-}}{\sum \lambda_i C_i}$, where λ_i is the ion molar conductivity at infinite dilution and C_i is the concentration of each ion. The transport numbers for all the ions are summarized in Table S1.

The current density to be applied in the trials was determined from a dimensionless number correlation (Eq. (5)) obtained experimentally in our recently published work [25], which informs about the hydrodynamic regime and the overall properties of the solution. Since the Sherwood number (*Sh*) correlates the convective mass transport with molecular diffusion ($Sh = k_m d_{RCE}/D_{NO_3^-}$) and, in turn, the mass transport coefficient (k_m) can be correlated to the limiting current density (j_L) for NO$_3^-$ electroreduction through $k_m = j_L/nFC_{NO_3^-}$, Eq. (5) can be rewritten as Eq. (6) to finally calculate the limiting current density for nitrate electroreduction under mass transport control.

$$Sh = 0.7 Re^{0.46} Sc^{0.356} \tag{5}$$

$$j_L = \frac{0.7 nFC_{NO_3^-} D_{NO_3^-}}{d_{RCE}} Re^{0.46} Sc^{0.356} \tag{6}$$

where j_L is in A m^{-2}, n is the number of electrons transferred in the global reduction reaction (=8), F is the Faraday constant (96,485 C mol^{-1}), $C_{NO_3^-}$ is the nitrate concentration (in mol m^{-3}), $D_{NO_3^-}$ is the nitrate diffusion coefficient (in m^2 s^{-1}), and d_{RCE} is the diameter of the RCE (0.038 m), whereas *Re* and *Sc* are the Reynolds ($Re = U d_{RCE}/\nu$, where ν is the kinematic viscosity of the fluid) and Schmidt ($Sc = \nu/D_{NO_3^-}$

= 463) dimensionless numbers, respectively. Table 1 shows the j_L values required at each peripheral velocity. It is important to mention that the index and the superscript values shown in Eq. (5) (0.7 and 0.46, respectively) are specific to this electrochemical system because it is an empirical equation. The former depends on the transport properties and the latter on the flow pattern [31]. Nonetheless, this kind of correlation has relevant implications in practice, since it eases the appropriate scale-up of the electrocatalytic nitrate removal if the diffusion-charge transfer characteristics are maintained (i.e., use of an RCE reactor under turbulent flow to treat nitrate solutions with comparable physicochemical properties).

The overall energy consumption (EC) of the electrolysis per gram of nitrate removed, was calculated as follows:

$$EC\,(Wh\,g^{-1}) = \frac{E_{cell} It}{3600(C_0 - C_t)MV} \tag{7}$$

where C_0 is the initial nitrate concentration, C_t is the nitrate concentration at each sampling time, V is the volume of the treated solution, I is the applied current (in A), t is the electrolysis time (in s), E_{cell} is the cell voltage (in V), and M is the molecular mass of nitrate ion (62 g mol^{-1}). It is worth mentioning that the duration of each trial was of 2 h and each of them was performed twice. Error bars are shown in the required figures.

2.3. Analytical methods

Nitrate concentration was quantified by ion chromatography using a Shimadzu 10Avp liquid chromatograph that comprised a Shim-Pack IC-A1 anion column, with dimensions of 100 mm × 4.6 mm (i.d.), kept at 40 °C and coupled to a Shimadzu CDD 10 Avp conductivity detector. This analysis was carried out by injecting 20 μL of the sample upon elution of a mobile phase composed of a 2.4 mM *tris*(hydroxymethyl) aminomethane solution at pH 4 + 2.6 mM phthalic acid solution at 1.5 mL min^{-1}. The ammonia concentration (in the form of ammonium ion) was determined via the standard indophenol blue colorimetric method, which allowed measuring the absorbance at λ = 645 nm in a UV4 Unicam UV/Vis spectrophotometer [16,17]. Total nitrogen (TN) measurements were performed in the TNM-1 unit coupled to a Shimadzu VCSN TOC analyzer. The electrochemical characterization of nitrate reduction and oxygen evolution reaction (OER) was performed by linear sweep voltammetry (LSV) in a standard three-electrode cell connected to an Autolab PGSTAT100 potentiostat. The working electrode was either an AISI 1018 steel or a Ti|IrO$_2$-based piece, for cathodic and anodic sweeps, respectively. A Pt rod and Ag|AgCl (3 M KCl) served as the counter and reference electrodes.

3. Formulation of the numerical simulation

In a previous communication, we described the experimental characterization of the RCE reactor for nitrate removal under potentiostatic conditions [25]. In that work, a dimensionless correlation was obtained to describe the electroreduction process, which can be used to calculate different parameters of the process to scale-up or improve the removal of nitrate. Nonetheless, this correlation offers little information about the intrinsic behavior of the RCE reactor in terms of hydrodynamics, mass transport and current distribution. Therefore, a model able to describe the phenomena occurring inside the reactor would ease the characterization of the reaction environment, allowing the enhancement of the reactor performance.

The modeling and simulation of NO$_3^-$ electroreduction in an RCE reactor compels to address the most critical aspects of this electrochemical system to obtain reliable results for hydrodynamics, mass transport and current distribution behavior. Thus, the governing equations for each phenomenon must be solved by proposing boundary conditions that accurately describe the motion of the central cylinder and the main properties of the solution. Moreover, the electrochemical

process must be well understood, since the electrochemical reactions depend on the kinetic parameters arising from the current applied to the specific electrocatalytic materials used as electrodes, as well as on the composition of the solution.

3.1. Electrochemical process

Nitrate electroreduction consists of two steps: (i) The two-electron reduction reaction (2) that converts nitrate to adsorbed NO_2^- on the cathode surface; and (ii) the subsequent six-electron complex cascade mechanism that reduces NO_2^- to either NH_3 from reaction (3) or N_2 from reaction (4). Since reaction (2) is established as the rate-determining step, the subsequent electron transfer to the adsorbed NO_2^- is comparatively fast. On this basis, NO_3^- electroreduction can be actually considered an eight-electron process, which in the case of carbon steel cathode results in the complete conversion to ammonia according to the global Eq. (8) [16,17]. At Ti|IrO$_2$-based anodes, the OER (reaction (9)) occurs concomitantly, without ammonia reoxidation [16,17].

$$NO_3^- + 6H_2O + 8e^- \rightarrow NH_3 + 9OH^- \tag{8}$$

$$4H_2O \rightarrow 2O_2 + 8H^+ + 8e^- \tag{9}$$

The overall reaction (8) can then be considered for simulation purposes, allowing to model the quick reduction of nitrate into ammonia on the cathode surface.

3.2. Turbulent model

RCE reactors can promote turbulence at relatively low rotation rates, reaching critical Re values in the range of 50–300, which promotes fluid instability and generation of eddies, thereby requiring to solve a set of equations that correctly describe the turbulent behavior [31]. To achieve the latter, a two-equations κ-ε model based on the Reynolds-averaged Navier-Stokes (RANS) equations was proposed. The κ-ε is a sophisticated turbulent model (and hence, more complex because it requires high computational efforts) that allows the description of turbulence through the effect of the generation (κ) and dissipation of turbulent kinetic energy (ε) [23,49]. Furthermore, this model has been widely used to characterize the RCE reactor by CFD due to its detailed description of turbulence, which results in outstanding theoretical trends that replicate very well the experimental results [35,36,44].

Therefore, the hydrodynamic model consisted in finding the solution of the RANS and continuity Eqs. (10) and (11) [49]. The electrolyte is an incompressible fluid, and the modeling considers isothermal and steady-state conditions. The turbulent viscosity (μ_T) is given by Eq. (12); hence, the κ-ε model equations are implemented within this term considering that the ratio between Reynolds stresses and mean rate of deformation is identical in all directions [49]. Both κ and ε are described by Eqs. (13) and (14), which must be solved simultaneously with Eqs. (10) and (11) to fully describe the turbulent phenomena:

$$\rho(\boldsymbol{u} \bullet \nabla)\boldsymbol{u} = -\nabla P + \nabla \bullet \left((\mu + \mu_T)\left(\nabla \boldsymbol{u} + (\nabla \boldsymbol{u})^T \right) \right) \tag{10}$$

$$\nabla \bullet \boldsymbol{u} = 0 \tag{11}$$

$$\mu_T = \rho C_\mu \frac{k}{\varepsilon} \tag{12}$$

$$\rho(\boldsymbol{u} \bullet \nabla)\kappa = \nabla \bullet \left(\left(\mu + \frac{\mu_T}{\sigma_\kappa} \right)\nabla\kappa \right) + P_\kappa - \rho\varepsilon \tag{13}$$

$$\rho(\boldsymbol{u} \bullet \nabla)\varepsilon = \nabla \bullet \left(\left(\mu + \frac{\mu_T}{\sigma_\varepsilon} \right)\nabla\varepsilon \right) + C_{\varepsilon 1}\frac{\varepsilon}{\kappa}P_\kappa - C_{\varepsilon 2}\rho\frac{\varepsilon^2}{\kappa} \tag{14}$$

where $\boldsymbol{u}$ is the average velocity vector, P is the averaged pressure, ρ is the density of the fluid, μ is the dynamic viscosity of the fluid, μ_T is the

turbulent viscosity, and P_k is an energy production term, whereas C_μ, $C_{\varepsilon 1}$, $C_{\varepsilon 2}$, σ_k and σ_ε are dimensionless empirical constants of the model [49].

In a turbulent regime, in the region close to the wall, the velocity of the fluid exponentially decreases as it approaches the viscous zone, where the turbulent model begins to disagree because it is strictly valid for high Re numbers. In this scenario, wall functions are often introduced to ensure that the simulation is done in the turbulent zone of the fluid. The most used wall function in the κ-ε turbulence model is described by Eq. (15).

$$u^+ = \frac{1}{k}\ln y^+ + 5.5 \tag{15}$$

where u^+ is the dimensionless velocity normal to the wall, k is the von Karman constant, and y^+ is the dimensionless distance from the wall to the turbulent zone [34,49].

In the RCE batch reactor, the solution motion is attributed solely to the RCE rotation; hence, to solve Eqs. (10)-(14), the following boundary conditions were set:

- At the RCE, the cathode rotation was chosen as a normal stress derived from the tangential velocity vector at the RCE surface, $\left[(\mu + \mu_T)\left(\nabla \bullet \boldsymbol{u} + (\nabla \bullet \boldsymbol{u})^T \right) \right]\boldsymbol{n} = -\rho\frac{u_\tau}{u^+}\boldsymbol{u}_{tang}$, where $u_\tau = C_\mu^{0.25}\sqrt{\kappa}$, $\boldsymbol{u}_{tang} = \boldsymbol{u} - \frac{\boldsymbol{u}_\omega - (\boldsymbol{u}_\omega \bullet \boldsymbol{n})\boldsymbol{n}}{\|\boldsymbol{u}_\omega - (\boldsymbol{u}_\omega \bullet \boldsymbol{n})\boldsymbol{n}\|}\|\boldsymbol{u}_\omega\|$, and $\boldsymbol{u}_\omega$ is the velocity vector of the moving RCE given by $2\pi\omega r_{RCE}$, where ω is in rev s^{-1} [44].
- At the open fluid surface, a decreasing shear stress is set to restrain the free movement of the fluid, $\left[(\mu + \mu_T)\left(\nabla \bullet \boldsymbol{u} + (\nabla \bullet \boldsymbol{u})^T \right) \right]\boldsymbol{n} = 0$, $\boldsymbol{u} \bullet \boldsymbol{n} = 0$, as the RCE reactor is open to the atmosphere.

To solve Eqs. (13) and (14), the following boundary conditions were set:

- At the open atmosphere surface, $\kappa = 0$ and $\varepsilon = 0$.
- In all remaining walls (including the electrodes), $\kappa = \frac{u_\tau^2}{\sqrt{C_\mu}}$ and $\varepsilon = \frac{u_\tau^3}{ky}$.

3.3. Mass transport

In turbulent regime in the absence of migration, ensured by the addition of a supporting electrolyte that allowed neglecting that term in the Nernst-Planck equation, the nitrate transport towards the RCE can be assessed by solving the time-dependent diffusion-convection Eq. (16) considering a turbulent diffusion coefficient (D_T):

$$\frac{\partial C_{NO_3^-}}{\partial t} = -\boldsymbol{u} \bullet \nabla C_{NO_3^-} + \nabla \bullet \left(D_{NO_3^-} + D_T \right)\nabla C_{NO_3^-} \tag{16}$$

where $\boldsymbol{u}$ is the average velocity vector obtained by solving Eqs. (10)-(14). The value of D_T can be calculated from the turbulent Schmidt number ($Sc_T = \mu_T/\rho D_T$). For this, the Kays-Crawford model of Eq. (17) was used.

$$Sc_T = \left\{ \frac{1}{2Sc_{T\infty}} + \frac{0.3\mu_T}{\sqrt{Sc_{T\infty}}\rho D} - \left(\frac{0.3\mu_T}{\rho D} \right)^2 \left[1 - exp\left(-\frac{\rho D}{0.3\mu_T\sqrt{Sc_{T\infty}}} \right) \right] \right\}^{-1} \tag{17}$$

where $Sc_{T\infty} = 0.85$ was included during the simulation of the diffusion-convection Eq. (16), to obtain D_T considering the local values of Sc_T and μ_T.

Although the current density at each rotation rate was calculated considering mass transport control, i.e., the concentration at the cathode surface is zero, the turbulent phenomena affecting the mass transport near the wall cannot be neglected. In this scenario, the Launder-Spalding model describes the concentration near the wall through a dimension-

Table 2

Electrolyte properties and kinetic parameters employed in the simulation of nitrate electroreduction in the RCE reactor.

Parameter	Symbol	Value	Unit
Fluid density	ρ	1000	kg m^{-3}
Fluid dynamic viscosity	μ	0.001	Pa s
Fluid kinematic viscosity	ν	1×10^{-6}	m^2 s^{-1}
Solution conductivity	σ	5.0	S m^{-1}
Nitrate diffusion coefficient	$D_{NO_3^-}$	1.9×10^{-9}	m^2 s^{-1}
Cathodic open circuit potential	OCP$_c$	-0.63	V (vs. SHE)
Anodic open circuit potential	OCP$_a$	0.68	V (vs. SHE)
Nitrate exchange current density	j_{0,NO_3^-}	0.67	A m^{-2}
HER exchange current density	j_{0,H_2^-}	0.18	A m^{-2}
OER exchange current density	$j_{0,OER}$	5.6×10^{-7}	A m^{-2}
Nitrate Tafel slope	$b_{NO_3^-}$	0.217	V
HER Tafel slope	b_{HER}	0.127	V
OER Tafel slope	b_{OER}	0.069	V

less concentration (C^+) at a distance y^+ by Eqs. (18) and (19), linking the viscous region with the turbulent zone [50]:

$$C_{NO_3^-}^+ = Sc_T \left(\frac{1}{k} \ln y^+ + 5.5 + P_c \right) \tag{18}$$

$$C_{NO_3^-}^+ = \frac{\left(C_{NO_3^-,w} - C_{NO_3^-} \right) C_\mu^{0.25} \kappa^{0.5}}{N_{NO_3^-,w}} \tag{19}$$

where $C_{NO_3^-}^+$ is the dimensionless nitrate concentration, $C_{NO_3^-,w}$ is the nitrate concentration in the region near the wall, $N_{NO_3^-,w}$ is the nitrate flux towards the RCE wall, and P_c is a factor that describes the resistances near the wall by Eq. (20):

$$P_c = A \left[\left(\frac{Sc}{Sc_T} \right)^{0.75} - 1 \right] \tag{20}$$

where A is an empirical constant fitted with a value in the range of 0–1 to adjust the experimental data. The mass transport wall function was employed to describe the rate of nitrate transport towards the RCE.

The corresponding boundary conditions to solve Eq. (16) were set as follows:

- At the RCE, a nitrate flux expressed as $-D_{NO_3^-} \frac{\partial C_{NO_3^-}}{\partial \xi} = N_{NO_3^-} = \frac{j_{0,NO_3^-} \left(\frac{C_{NO_3^-,w}}{C_{NO_3^-}} \right) \exp \left(\frac{\eta_{NO_3^-}}{b_{NO_3^-}} \right)}{nF}$, where j_{0,NO_3^-} is the exchange current density for nitrate reduction, $b_{NO_3^-}$ is the Tafel slope for nitrate reduction, and $\eta_{NO_3^-}$ is the nitrate reduction overpotential calculated as $\eta_{NO_3^-} = \varphi_M - \varphi - OCP_c$, where φ_M is the electrode potential, φ is the electric potential adjacent to the electrode, and OCP$_c$ is the cathodic open circuit potential (see Table 2).
- In all the remaining walls, a zero-flux condition is set.

The initial condition to solve Eq. (16) is stated as follows:

- At $t = 0$, $C_{NO_3^-} = C_{NO_3^-}(t = 0)$, i.e., the initial nitrate concentration.

3.4. Tertiary current in the RCE reactor

In an electrochemical process, the reactions are conditioned by the current density and the potential applied to the electrode. The Laplace equation describes the electric potential distribution in the solution from Eq. (21). Conversely, the electrode local current density can be calculated through the Ohm's law of ionic conductance, Eq. (22).

$$\nabla \varphi^2 = 0 \tag{21}$$

$$j = -\sigma \nabla \varphi \tag{22}$$

where φ is the electric potential, j is the current density vector, and σ is the ionic conductivity of the solution.

Eq. (21) is solved by considering the following boundary conditions:

- At the RCE, an overall cathodic current density is set, including the nitrate reduction as well as the HER, $-\sigma \frac{\partial \varphi}{\partial \xi} = j_c = j_{0,NO_3^-} \left(\frac{C_{NO_3^-,w}}{C_{NO_3^-}} \right) \exp \left(\frac{\eta_{NO_3^-}}{b_{NO_3^-}} \right) + j_{0,HER} \exp \left(\frac{\eta_{HER}}{b_{HER}} \right)$, where b_{HER} and η_{HER} are the Tafel slope and overpotential attributed to HER, respectively. Both reactions are considered because of the co-occurrence of nitrate electroreduction [25].
- At the anodes, Tafel approach is defined as $-\sigma \frac{\partial \varphi}{\partial \xi} = j_a = j_{0,OER} \exp \left(\frac{\eta_{OER}}{b_{OER}} \right)$, where $j_{0,OER}$, b_{OER} and η_{OER} are the exchange current density, Tafel slope and overpotential attributed to OER, respectively.
- At the remaining insulating walls, a zero-flux condition is set.

Noticeably, the concentration overpotential $\left(\frac{C_{NO_3^-,w}}{C_{NO_3^-}} \right)$ is present in the boundary conditions related to the RCE in Eqs. (16) and (21) because mass transport and potential distribution depend on each other. The dependence on the nitrate concentration near the wall in both conservation equations compels the simultaneous solution of the mass transport and current distribution models. It is worth mentioning that, to include the phenomena occurring near the RCE wall as described in Eqs. (18)-(21), the nitrate concentration was considered near zero on the wall. This allows describing more accurately the process. Also, to solve Eqs. (16), (21), and (22), the φ_M value was fixed to obtain a total current density at the electrodes, used to simulate the applied current density corresponding to the experimental nitrate electroreduction.

3.5. Simulations

The conservation equations described in this model were solved by means of the finite element method, employing COMSOL Multiphysics® 6.0 software on a computer with two Intel® Xeon™ 2.30 GHz processors (96 GB RAM, 64-bit operating system). With the correct selection of the physics and set of boundary conditions, the COMSOL Multiphysics® software is able to solve the conservation equations linked to the transport of momentum (hydrodynamics) and mass (diffusion-convection), as well as to potential distribution to obtain reliable data able to replicate the experimental behavior of the nitrate electroreduction in the RCE reactor.

The hydrodynamics model was solved with an iterative GMRES method with a relative tolerance of 1×10^{-3} in a stationary state. On the other hand, the mass transport and the potential distribution models were solved simultaneously using the same iterative method in a time-dependent solver considering a time step of 300 s for a simulation that lasted 1800 s. An averaged nitrate concentration was calculated in each time step to depict the nitrate decay curve from the simulations. Simulations of hydrodynamics took ca. 180 min, whereas the time-dependent model could be solved in 120 min for a total simulation time of approximately 300 min per simulation. Table 2 shows the electrolyte properties and electrochemical kinetic parameters needed for the simulations. It is worth mentioning that the exchange current densities and Tafel slopes used in this work were obtained through LSV analysis carried out with the specific electrode materials, as shown in Fig. S1. The specific kinetic parameters for nitrate electroreduction correspond to the process occurring in concomitance with HER, since it has been demonstrated in our previous work [25] that both reactions are coupled through atomic hydrogen that acts as mediator of NO$_3^-$ reduction.
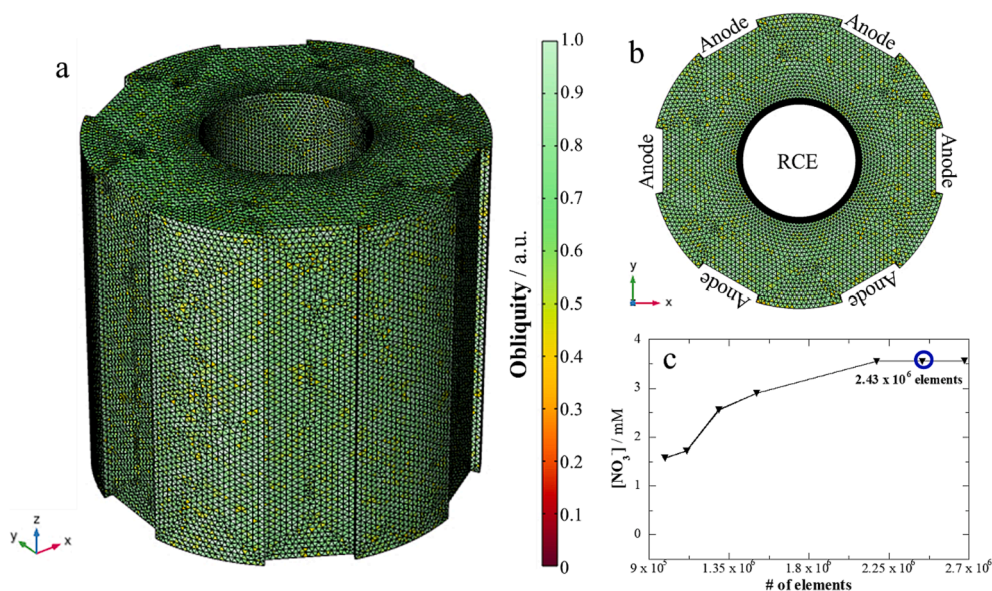
Fig. 1. (a) Isometric view of the simulation domain with the field of element quality in the mesh. (b) Upper view of the simulation domain with the position of each electrode. (c) Mesh sensitivity analysis performed by determining the nitrate concentration at 5 min of simulation time. Simulation parameters: 10 mM NO$_3^-$ at 25 °C, operating and 300 rpm.

Fig. 1a shows an isometric view of the simulation domain, i.e., the RCE reactor, with the field of element quality throughout the domain. The mesh consisted of 2.43×10^6 tetrahedral elements with an average quality above 0.66. Fig. 1b shows the upper view of the simulation domain with the electrode arrangement employed in the simulations; the RCE is placed at the center and six anode plates surround it. Fig. 1c shows the sensitivity analysis performed for the NO$_3^-$ electroreduction considering its concentration at 5 min of simulation time at 300 rpm. Several simulations were performed by changing the element size to improve the accuracy of simulations; optimum reproducibility of results was achieved with a mesh consisting of 2,178,025 elements. Nonetheless, the mesh consisting in 2,436,728 elements was selected to obtain a more detailed solution in the region near the RCE, requiring similar computation times of 290 and 300 min, respectively.

4. Results and discussion

### 4.1. Simulation of the turbulent regime

By solving the conservation equations that govern the momentum transport, Eqs. (10)-(14), both the overall behavior and local values of velocity can be obtained. Fig. 2a shows an upper view of a set of 58 surface arrows that was obtained at $z = 4$ cm (i.e., in the middle of the reactor length) that inform about the rotation of the fluid elements in a clockwise direction. This can be explained by the tangential velocity boundary condition set on the RCE surface simulating the movement of the liquid towards the center of the reactor. The latter can be confirmed by the fact that the velocity tends to increase near the RCE and has a homogeneous profile around the perimeter of the electrode. On the other hand, due to the clockwise rotation, low-velocity zones are noticed in the corners of each anode, since the elements of the fluid are slowly dragged into the bulk.

Moreover, Fig. 2b shows an isometric view of the velocity field on the surface of the RCE reactor. It can be observed that in the upper part of the reactor, the velocity values are higher when compared to the cut at the center of the reactor. Additionally, two low-velocity zones can be distinguished on the reactor outer walls at $z = 0$ and 5.4 cm. The presence of such lower velocity zones can be accounted for by the presence of two Taylor vortices, as can be seen in Fig. 2c, at z values of 2.9 and 8.0 cm. These toroidal vortices are generated because the anodes act as deflectors of the fluid within the reactor, thus modifying the trajectory of the fluid elements into a more chaotic and unstable pattern. Fig. 2c
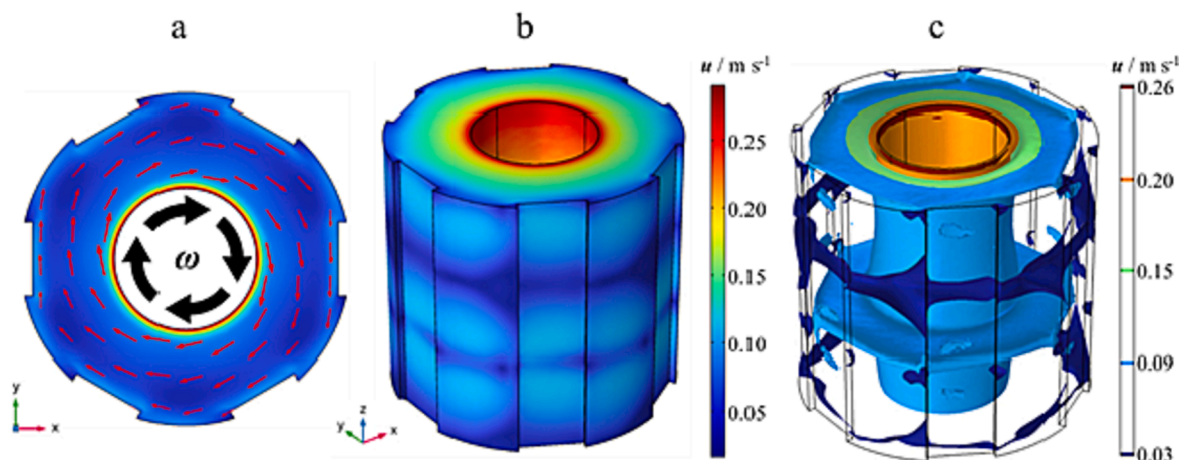

Fig. 2. (a) Velocity field inside the RCE reactor in the xy-plane at $z = 4.0$ cm. (b) Isometric view of the velocity field on all boundaries of the RCE reactor. (c) Five levels of isosurface within the RCE reactor. Simulation parameters: water at 25 °C, operating at 300 rpm.
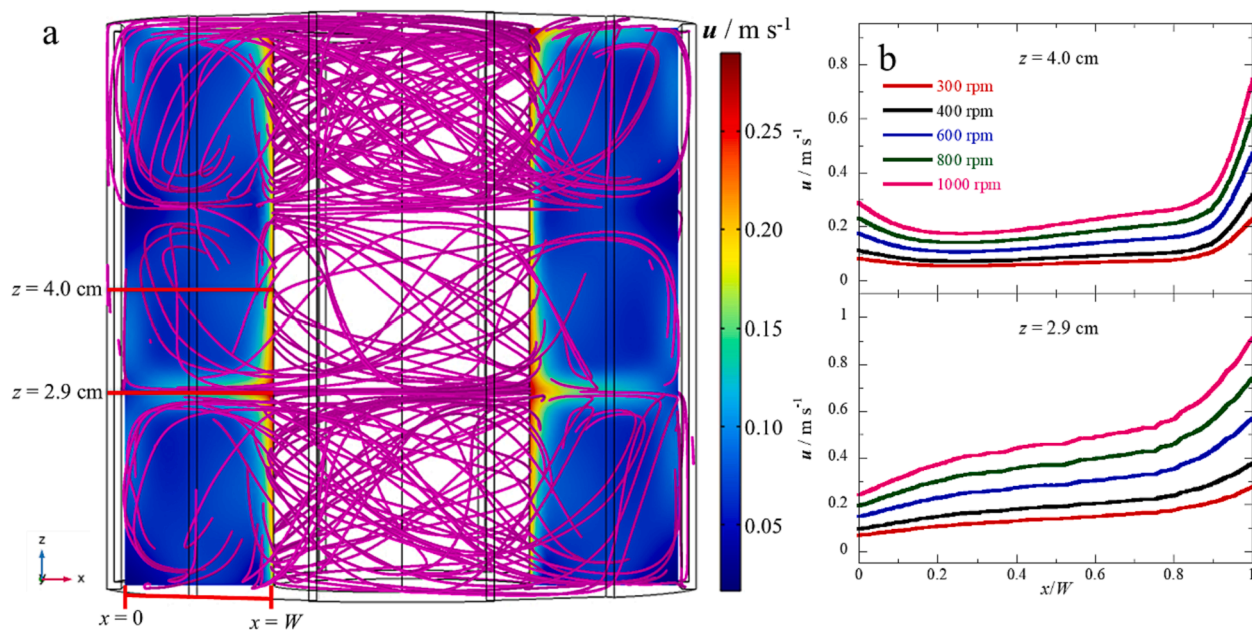
Fig. 3. (a) Set of 50 streamlines and plane cut of the RCE reactor. (b) Velocity profiles evaluated between an anode and the RCE, at two heights (z): 2.9 and 4.0 cm. Simulation parameters: water at 25 °C, operating at 300 rpm.
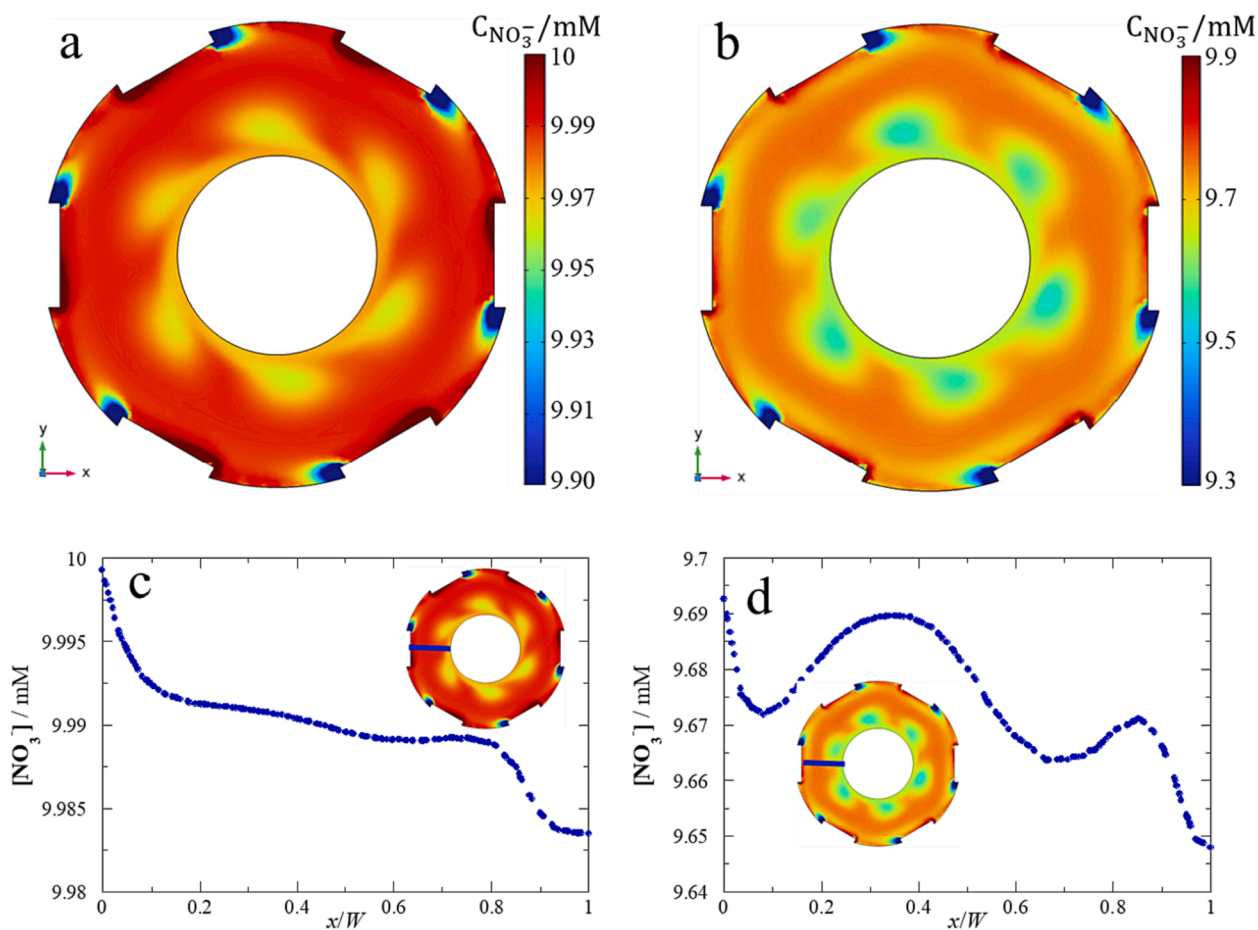
Fig. 4. Influence of the rotation rate on the nitrate concentration field within the RCE reactor: (a) 300 rpm and (b) 1000 rpm. Concentration profile from the anode to the RCE, at (c) 300 rpm and (d) 1000 rpm. Simulation parameters: 10 mM NO_3^- at 25 °C. Data obtained at 5 s of simulation time.
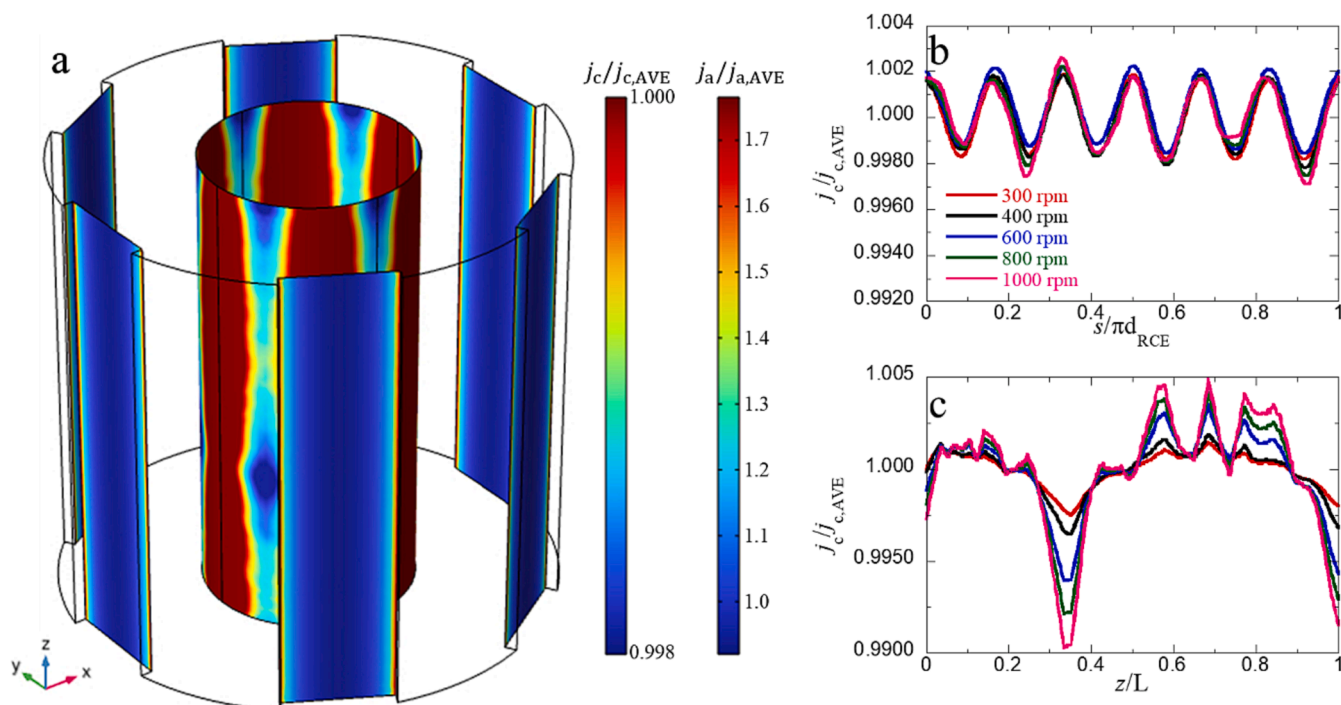
Fig. 5. (a) Normalized current density distribution field on the RCE and the six anodes. The same simulation parameters as those of Fig. 4 at 300 rpm were used. Normalized current density distribution (b) along the normalized RCE arc length at $z = 8.0$ cm, and (c) along the normalized RCE length where the electrode is facing an anode, at different rotation rates.
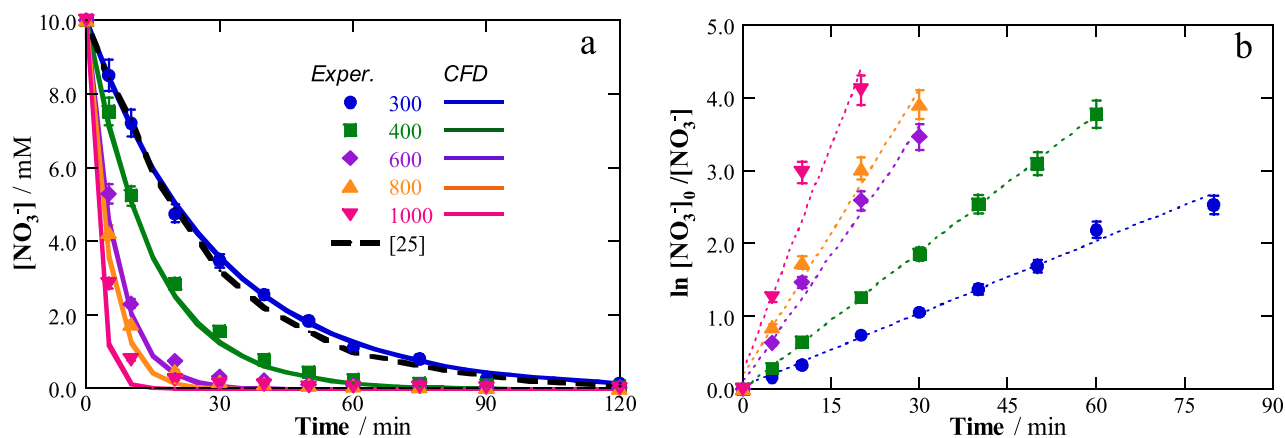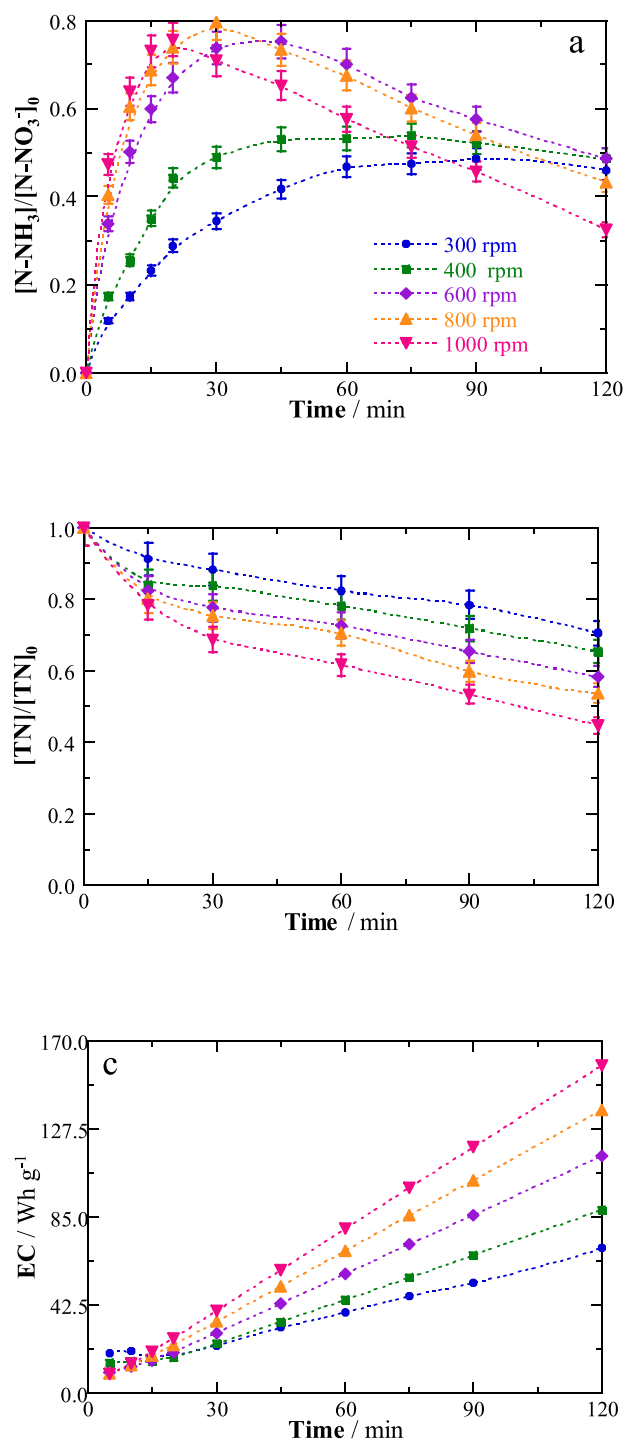

Fig. 6. Influence of the rotation rate on (a) nitrate electroreduction and (b) the resulting first-order kinetics. Experimental results and simulations are compared. The dotted line corresponds to the nitrate electroreduction in an experiment done previously with similar experimental parameters under potentiostatic condition (E_{cath} = −1.8 V vs. SHE) [25]. Solution: 10 mM KNO$_3$ + 500 mM K$_2$SO$_4$ at 25 °C. The applied densities are linked to each rotation rate (see Table 1) to guarantee mass transport control.

shows a set of five isosurfaces from the slowest to the highest velocity inside the reactor, which confirms the presence of the low-velocity zones as well as the Taylor vortices, and the increasing velocity as the fluid is closer to the RCE surface. The number of Taylor vortices in an RCE reactor depends on the geometrical aspects (height and diameter), the electrode arrangement, the reactor volume, and the surface boundary condition set (closed or open to the atmosphere). Usually, for RCE reactors operating in batch mode, one, two, or three Taylor vortices are reported. Colli and Bisang [45] solved a 2D-axisymmetric RCE model that considered a concentric outer electrode, finding a single Taylor vortex in the middle of the reactor. In that work, it was concluded that the Taylor vortex enhanced the mass transport toward the electrode surface because the *Sh* number increased in the zones where the vortex was detected. Moreover, in the work reported by Rivero et al. [36], an

RCE reactor with similar geometry (d_{RCE} = 3.8 cm) was employed to describe Cu deposition. In that work, three Taylor vortices promoted by the RCE were observed; this divergence in the number of Taylor vortices using a similar reactor could be due to slight differences in the simulation domains, e.g., the thickness of the counter electrodes, the length of the RCE or the interelectrode gap. In contrast, a work published by Villalobos et al. [51] developed a model of an RCE reactor with a non-fully submerged RCE, i.e., the electrode was over the bottom of the vessel, which drastically changed the hydrodynamic behavior at the bottom of the reactor to yield two Taylor vortices. Even though RCE reactors can be geometrically similar, the phenomena occurring within them can be influenced by small variations, such a wider/narrower gap between electrodes, RCE positioning and reactor volume. Nonetheless, all reported works agree with the higher capacity of RCE reactors to

Fig. 7. Influence of the rotation rate on (a) normalized ammonia accumulation, (b) normalized total nitrogen depletion, and (c) energy consumption during the nitrate electroreduction process. The same experimental parameters as in Fig. 6 were used.

promote turbulence and enhance the efficiency of electrochemical processes.

Fig. 3a shows a set of 50 streamlines within the RCE reactor, highlighting that the presence of the Taylor vortices at z values of 2.9 and 8.0 cm promotes the appearance of three distinct zones within the RCE reactor. Near the RCE, it can be observed that the elements of the fluid move around it. On the other hand, as the fluid gets closer to the anodes, a back mixing starts to develop as the anodes act as fluid deflectors. The first two zones can be attributed to this phenomenon caused by the first

Taylor vortex. In contrast, the third zone can be correlated with the collision of the chaotic behavior generated by both vortices. The velocity profile from the anode surface ($x = 0$) to the RCE one ($x = W = 2.1$ cm), being x/W the normalized distance between electrodes ranging between 0 and 1 for the anode and cathode positions, respectively, can be obtained at different heights on the z-coordinate to elucidate the velocity evolution in the anode–cathode gap. Fig. 3b shows the velocity profile in the electrode gap at z values of 2.9 and 4.0 cm, which correspond to the position of the first Taylor vortex and the center of the reactor, respectively, at different rotation rates. At $z = 2.9$ cm, the velocity increases steadily across the anode-to-cathode gap due to the increased acceleration promoted by the Taylor vortex, with a steeper increment at $x/W = 0.85$, where the inertial force of the RCE is more prominent. On the other hand, at $z = 4.0$ cm, the velocity of the fluid remains practically unchanged between $0.1 < x/W < 0.9$ due to the homogeneous velocity field promoted at the reactor center and between both Taylor vortices. Nonetheless, similarly to the behavior observed at $z = 2.9$ cm, the velocity increases exponentially at $x/W = 0.9$ due to the forced convection imposed by the RCE.

4.2. Mass transport and tertiary current distribution simulations

As discussed above, mass transport is closely linked to the hydrodynamic pattern, since the species in the reactor reach the electrode surface due to the rotation of the RCE. In turn, the potential distribution is affected by the local concentration of the species within the reactor. In an RCE reactor, the contribution of the convective term in Eq. (16) is higher than that of the diffusion term, which enhances the mass transport rate that in consequence promotes a uniform tertiary current distribution, i.e., the concentration gradient is relevant. Fig. 4a and 4b show the nitrate concentration field at 300 and 1000 rpm after 5 s of simulation time. It can be noticed that in the corner of each anode, the nitrate concentration is lower than in the bulk due to the low velocity, which makes difficult for the nitrate to reach or leave these zones. Moreover, in the inner part of the reactor, the concentration has an almost unchanged value of 9.98 and 9.60 mM, respectively, resulting from the stirred tank behavior, which favors the homogeneity of the properties in the bulk.

Additionally, as the fluid approaches the RCE, the concentration value decreases. It is worth noticing the presence of six notorious forms around the RCE, which arise from the deflector-like pattern produced by the anodes, accelerating the fluid in the clockwise rotation. These zones penetrate more into the bulk volume at 1000 rpm, since the higher rotation rate, the more chaotic and faster the fluid becomes, which also accelerates the concentration decay at the cathode surface. The latter can be assessed in Fig. 4c, where it can be observed that, at 300 rpm, the concentration follows a quite linear path from the bulk near the anode to a distance $x/W = 0.8$, where the concentration depletes faster on the RCE surface. On the other hand, Fig. 4d elucidates the more chaotic concentration profile as the RCE is approached. A slight increase of the nitrate concentration is attained near the anode surface, which then continuously depletes until the anion reaches the RCE surface. These trends are in good agreement with the faster dragging of nitrate toward the cathode when the rotation rate is increased in the RCE reactor. It is also worth noting that D_T inside the reactor had values in the range of $8–24 \times 10^{-6}$ m^2 s^{-1} at 300 rpm, as shown in Fig. S2; the highest values are found at the center of the interelectrode gap, where the velocity increases, and they decrease toward the electrode surface because of the velocity decay. The values of D_T are three orders of magnitude higher than that of $D_{NO_3^-}$ (1.9×10^{-9} m^2 s^{-1}), which confirms the much higher influence of turbulence as compared to molecular diffusion to transport nitrate anion inside the RCE reactor. On the other hand, the values of Sc_T obtained were in the range of $0.81 \leq Sc_T \leq 0.89$ at 300 rpm, as depicted in Fig. S2. This agrees with typical values ranging between 0 and 1 [45,52]. Here, it is worth reminding that in our previous work, the
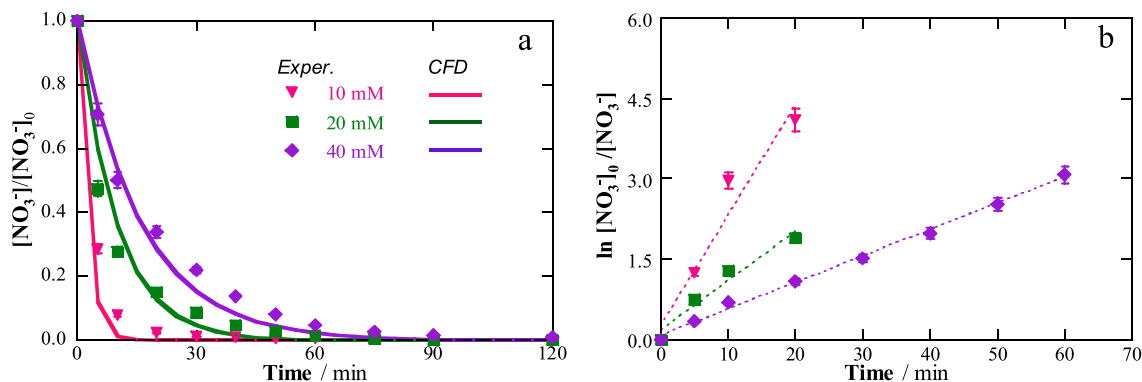
Fig. 8. Influence of nitrate initial concentration on (a) normalized nitrate depletion and (b) the resulting first-order kinetics. Experimental results and simulations are compared. All electrolyses were made in 500 mM K_2SO_4, at 25 °C and 1000 rpm (i.e., $j_L = 447$ A m^{-2}).

comparison between the intrinsic kinetic rate constant and overall mass transport in terms of k_m confirmed that the process is controlled by mass transport [25].

The current distribution is a crucial parameter to assess in electrochemical reactors, since it is highly desirable that the current values are equal at any point of the electrode surface. Commonly, the current distribution is reported as a ratio between the local current (j) and the average current (j_{AVE}) on the electrode surface and, if $j/j_{AVE} \sim 1$, it means that the current is distributed homogeneously on the whole electrode. In this context, the six anodes show a current distribution near the isolating walls, increasing the value of $j_a/j_{a,AVE}$ up to 1.7, which is attributed to the position of the electrodes regarding the isolating walls (Fig. 5a). On the other hand, the RCE shows a lower current distribution of $j_c/j_{c,AVE} = 0.998$ in the areas where the electrode is not facing an anode (Fig. 5a). In contrast, as long as the RCE faces an anodic plate, the current tends to $j_c/j_{c,AVE} \sim 1$ along all the cylinder. Fig. 5b shows the normalized current distribution at $z = 8.0$ cm as a function of the normalized arc length ($s/\pi d_{RCE}$) for the range of $300 < \omega < 1000$ rpm. This distribution on the RCE surface ranges between $0.998 < j_c/j_{c,AVE} < 1.002$. This variation is due to the electrode arrangement that results in a slight current distribution when facing the insulating walls. The latter finding agrees with that attained in a previous paper on the simulation of current distribution at the RCE during copper electrodeposition [53]. Moreover, Fig. 5c shows that the normalized current distribution along the RCE length has values between $0.990 < j_c/j_{c,AVE} < 1.005$, showing a moderate current distribution. At each rotation rate, the largest variations from that number are observed at z/L of 0.34 and 1.0 (i.e., $z = 2.9$ and 8.0 cm, respectively), in good agreement with the presence of the two Taylor vortices that cause a velocity increase in those zones, thereby promoting a higher mass transport with a slight current distribution. Despite these observations, note that the current distribution detected around the RCE arc length and RCE length was always below 1 %, corroborating that this system is suitable to perform electrochemical processes.

4.3. Nitrate electroreduction

The experimental nitrate electroreduction trials were carried out in a 400-mL RCE reactor, assessing the influence of the rotation rate (300–1000 rpm) and the initial nitrate concentration (10–40 mM). The applied current density in each trial was between 26 and 45 mA cm^{-2}, directly depending on the rotation rate established by Eq. (6) as summarized in Table 1; these current densities corresponded to E_{cell} between 3.6 and 4.5 V. The electrochemical process is under mass transport control regime at high rotation, whereas at low and moderate rotations (i.e., current values), the system is controlled by a charge transfer and mass transport mixed regime [25]. The results of all electrolytic trials regarding the nitrate concentration were compared with the results

predicted by the mathematical model developed as explained in Section 3. Fig. 6a shows the influence of the rotation rate of the RCE on nitrate reduction. The faster the RCE rotates, the quicker the nitrate removal from the solution. At 300 rpm, the nitrate is removed in 120 min, whereas at 1000 rpm, 90 % of the nitrate in the solution is removed in 10 min. The accelerated electroreduction of nitrate as the rotation rate increases is more evident upon evaluation of the first-order kinetic constant (k_1). This parameter reached values of 3.37×10^{-2} min^{-1} ($R^2 = 0.996$), 6.26×10^{-2} min^{-1} ($R^2 = 0.999$), 12.16×10^{-2} min^{-1} ($R^2 = 0.994$), 13.99×10^{-2} min^{-1} ($R^2 = 0.990$), and 22.47×10^{-2} min^{-1} ($R^2 = 0.995$) at 300, 400, 600, 800, and 1000 rpm, respectively. The k_1-value obtained at 1000 rpm is six-fold the one obtained at the lowest velocity, which confirms that when the nitrate is more quickly dragged toward the RCE, the electroreduction is favored at the electrode surface. At high rotations, the nitrate is continuously dragged toward the electroactive surface of the RCE, resulting in a higher amount of nitrate near the electrode interface. This accelerates the occurrence of the rate-determining step (reaction (2)) and the subsequent cascade sequence that begins with reaction (3). It is worth mentioning that the nitrate profile obtained at 300 rpm is similar to that reported upon use of the RCE under potentiostatic conditions ($E_{cath} = -1.8$ V vs. SHE) at 300 rpm [25]. Furthermore, an excellent fitting between the experimental results and data simulated from the model proposed in Section 3 was achieved. Moreover, at $t < 30$ min, the calculated current efficiency for nitrate electroreduction was over 90 %, confirming the good performance of the RCE reactor to carry out the decontamination treatment.

Apart from the faster nitrate elimination attained at higher rotation rates due to resulting higher applied current densities and improved mass transport towards the cathode, the simultaneous assessment of the products generated is of particular interest. Fig. 7a shows the normalized profiles related to the NH_3 accumulation at each of the assessed ω values. The maximum accumulations attained were near 80 % at $\omega \geq 800$ rpm due to the quicker release of NH_3 into the bulk from the nitrate electroreduction, which is enhanced on the RCE surface. In addition, it can be observed that as the rotation rate rises from 600 to 1000 rpm, the maximum of the NH_3 accumulation appears at shorter times and has a steep depletion after 45, 30, and 15 min at 600, 800, and 1000 rpm, respectively. This abrupt depletion of NH_3 is explained by the increasing release of the generated NH_3 to the atmosphere at alkaline medium, since the volatilization of NH_3 is promoted according to Henry's law and an open RCE reactor was employed. The maximum values attained were 75 %, 80 %, and 76 %, which dropped at the end of the electrolysis to 49 %, 43 %, and 33 % at 600, 800, and 1000 rpm, respectively. On the other hand, at $\omega \leq 400$ rpm, a steady and lower accumulation of NH_3 attaining values of 49 % and 54 % at 300 and 400 rpm, respectively, was found due to the slower kinetics of the nitrate electroreduction leading to lower accumulations of NH_3 into the bulk. Moreover, the volatilization of the NH_3 at $\omega \leq 400$ was diminished by the hydrodynamics inside the
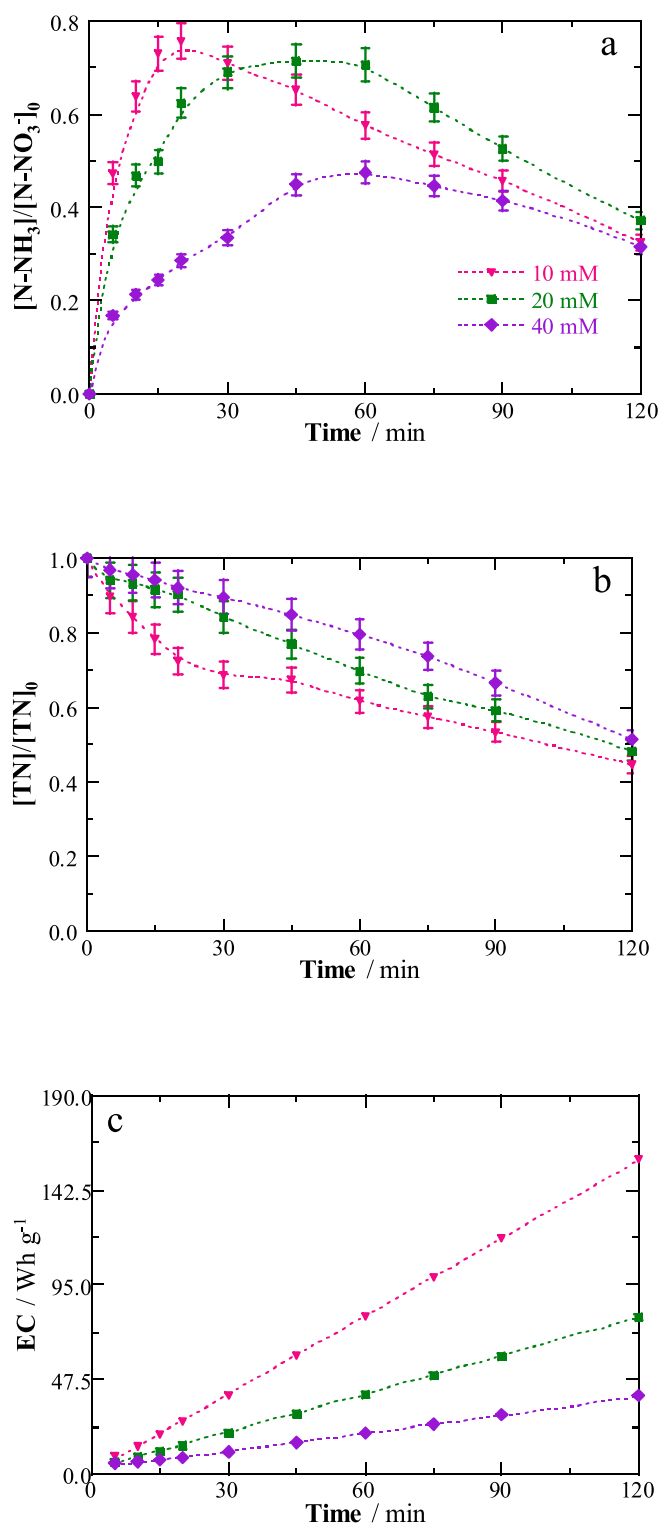
Fig. 9. Influence of nitrate initial concentration on (a) normalized ammonia accumulation, (b) normalized total nitrogen depletion, and (c) energy consumption during the nitrate electroreduction process. The same experimental parameters as in Fig. 8 were used.

RCE reactor, with final NH$_3$ values of 46 % and 49 % at 300 and 400 rpm, respectively. The increased release of N-species to the atmosphere as ω increases can be corroborated with the profiles of total nitrogen over the electrolysis time. Fig. 7b confirms the significant influence of ω on the volatilization of the N-species, since total nitrogen content decays steadily throughout the electrolysis time, reaching values of 30 %, 35 %,

4 %2, 46 %, and 55 % at 300, 400, 600, 800, and 1000 rpm, respectively.

Fig. 7c shows the EC values attained solely considering the nitrate electroreduction according to Eq. (8). It is noticeable in that figure that, at $t < 15$ min, lower values were attained at higher rotation rates. Nonetheless, at $t > 15$ min, the trends show that higher rotation rates yield greater EC values. These results can be justified by the low residual nitrate concentration throughout the electrolysis, which also favors secondary reactions such as HER.

Fig. 8a highlights the influence of the initial nitrate concentration on its electroreduction profile. As the initial concentration of nitrate increased, its complete removal required longer time, reaching its total disappearance after ca. 20, 60, and 75 min at 10, 20, and 40 mM NO$_3^-$, respectively. The k_1-values determined from the slopes of Fig. 8b were 22.5×10^{-2}, 7.9×10^{-2}, and 4.6×10^{-2} min^{-1}, respectively. Although the process is mostly under mass transport control, increasing the initial pollutant content in a highly efficient mass transport system like the RCE reactor resulted in a relatively slower nitrate removal process (i.e., lower k_1), although this entailed an enhanced overall nitrate removal rate. A first-order kinetic constant is not expected to depend on the concentration of the reactant when the electrolyses are performed at constant current (447 A m^{-2} in this case), but such k_1 decay was actually observed as the initial concentration of the electroactive species was increased. Note also that although the selected cathode material is proven to yield the total removal of nitrate even at high concentrations, other more electrocatalytic materials could be investigated to face the sluggish kinetics of nitrate electroreduction [25]. It is especially important to highlight that the theoretical and experimental results showed a good agreement, evidencing the robustness of the proposed nitrate electroreduction model to predict the process behavior in an RCE reactor equipped with an AISI 1018-type steel cathode.

The NH$_3$ accumulation is shown in Fig. 9a. It is noticeable that as the initial NO$_3^-$ concentration increased, it hindered the accumulation of NH$_3$ with maximum accumulation attained of 76 %, 71 %, and 48 % at 20, 45, and 60 min, respectively, at each increasing nitrate concentration. Also, the relative volatilization of N-species was slowed down as the nitrate initial concentration increased, owing to higher absolute accumulation rates. The overall percentage of NH$_3$ remaining at the end of the electrolysis was 33 %, 37 %, and 32 % at 10, 20, and 40 mM NO$_3^-$, respectively. The latter is confirmed in Fig. 9b because when the initial nitrate concentration increased, the volatilization of N-species was slower, reaching final TN removals of 55 %, 52 %, and 49 % as the nitrate concentration was risen from 10 to 40 mM NO$_3^-$.

Furthermore, the EC values shown in Fig. 9c increase linearly through the electrolysis time, reaching values of 39.8, 40.0, and 39.8 Wh g^{-1} for the abatement of 99 % of nitrate after 30, 60 and 120 min at 10, 20, and 40 mM NO$_3^-$, respectively.

5. Conclusions

The modeling and simulation of an electrochemical reactor equipped with an AISI 1018 carbon steel RCE used for nitrate electroreduction was performed successfully. The solution of the momentum equations gave rise to two Taylor vortices inside the RCE reactor due to the influence of the surrounding electrodes acting as deflectors and modifying the flow pattern. It was also determined that the RCE had a current distribution in the range of $0.990 < j_c/j_{c,AVE} < 1.005$ due to the two Taylor vortices. The model proposed was validated by adjusting the theoretical nitrate electroreduction with experimental results. Additionally, the fastest nitrate removal was achieved in a solution containing 10 mM NO$_3^-$ + 500 mM K$_2$SO$_4$ at 1000 rpm and 25 °C, requiring only 10 min for >90 % removal with an EC of 14.3 Wh g^{-1}. Also, ammonia was detected as the main product, and its volatilization caused by the increased pH accounted for 55 % removal of total nitrogen.

The results obtained show that a mathematical model can replicate the behavior of the RCE reactor for electrochemical nitrate removal controlled by mass transport at different rotation rates. The use of an

RCE reactor for nitrate electroreduction is a promising technology to address nitrate contamination due to its high conversion to ammonia.

CRediT authorship contribution statement

Roger Oriol: Writing – review & editing, Methodology, Investigation, Data curation. **José L. Nava:** Writing – review & editing, Validation, Funding acquisition, Data curation, Conceptualization. **Enric Brillas:** Writing – review & editing, Validation, Formal analysis. **Oscar M. Cornejo:** Writing – review & editing, Writing – original draft, Methodology, Investigation, Data curation. **Ignasi Sirés:** Writing – review & editing, Writing – original draft, Validation, Supervision, Resources, Project administration, Funding acquisition, Data curation, Conceptualization.

Declaration of competing interest

The authors declare the following financial interests/personal relationships which may be considered as potential competing interests: Ignasi Sires reports financial support was provided by State Agency of Research. If there are other authors, they declare that they have no known competing financial interests or personal relationships that could have appeared to influence the work reported in this paper.

Data availability

Data will be made available on request.

Acknowledgments

Appendix A. Supplementary material

Supplementary data to this article can be found online at https://doi.org/10.1016/j.seppur.2024.126714.

References

[1] B. Singh, E. Caswell, Fertilizers and nitrate pollution of surface and ground water: an increasingly pervasive global problem, SN Appl. Sci. 3 (2021) 518, https://doi.org/10.1007/s42452-021-04521-8.

[2] E. Abascal, L. Gómez-Coma, I. Ortiz, A. Ortiz, Global diagnosis of nitrate pollution in groundwater and review of removal technologies, Sci. Total Environ. 810 (2022) 152233, https://doi.org/10.1016/j.scitotenv.2021.152233.

[3] S. Singh, A.G. Anil, V. Kumar, D. Kapoor, S. Subramanian, J. Singh, P. C. Ramamurthy, Nitrates in the environment: A critical review of their distribution, sensing techniques, ecological effects and remediation, Chemosphere 287 (2022) 131996, https://doi.org/10.1016/j.chemosphere.2021.131996.

[4] O. Rahmati, A.N. Samani, N. Mahmoodi, M. Mahdavi, Assessment of the contribution of N-fertilizers to nitrate pollution of groundwater in western Iran (Case study: Ghorveh-Dehgelan aquifer), Water Qual. Expos. Health 7 (2015) 143–151, https://doi.org/10.1007/s12403-014-0135-5.

[5] J. Nemčić-Jurec, A. Jazbec, Point source pollution and variability of nitrate concentrations in water from shallow aquifers, Appl. Water Sci. 7 (2017) 1337–1348, https://doi.org/10.1007/s13201-015-0369-9.

[6] A. Menció, J. Mas-Pla, N. Otero, O. Regàs, M. Boy-Roura, R. Puig, J. Bach, C. Domènech, M. Zamorano, D. Brusi, A. Folch, Nitrate pollution of groundwater; all right…, but nothing else? Sci. Total Environ. 539 (2016) 241–251, https://doi.org/10.1016/j.scitotenv.2015.08.151.

[7] N. Adimalla, H. Qian, Groundwater chemistry, distribution and potential health risk appraisal of nitrate enriched groundwater: A case study from the semi-urban region of South India, Ecotox. Environ. Safe. 207 (2021) 111277, https://doi.org/10.1016/j.ecoenv.2020.111277.

[8] Y. Zhai, Y. Lei, J. Wu, Y. Teng, J. Wang, X. Zhao, X. Pan, Does the groundwater nitrate pollution in China pose a risk to human health? A critical review of published data, Environ. Sci. Pollut. Res. 24 (2017) 3640–3653, https://doi.org/10.1007/s11356-016-8088-9.

[9] S.M.K. Alam, P. Li, M. Fida, Groundwater nitrate pollution due to excessive use of N-fertilizers in rural areas of Bangladesh: Pollution status, health risk, source contribution, and future impacts, Expos. Health (2023), https://doi.org/10.1007/s12403-023-00545-0.

[10] Y. Fan, J. Zhuang, M. Essington, S. Jagadamma, J. Schwartz, J. Lee, Global significance of substrates for nitrate removal in denitrifying bioreactors revealed by meta-analysis, Eng. 21 (2023) 214–226, https://doi.org/10.1016/j.eng.2022.08.017.

[11] Y. Pang, J. Wang, Various electron donors for biological nitrate removal: A review, Sci. Total Environ. 794 (2021) 148699, https://doi.org/10.1016/j.scitotenv.2021.148699.

[12] Y. Liu, X. Zhang, J. Wang, A critical review of various adsorbents for selective removal of nitrate from water: Structure, performance and mechanism, Chemosphere 291 (2022) 132728, https://doi.org/10.1016/j.chemosphere.2021.132728.

[13] S. Meng, Y. Ling, M. Yang, X. Zhao, A.I. Osman, A.H. Al-Muhtaseb, D.W. Rooney, P. S. Yap, Recent research progress of electrocatalytic reduction technology for nitrate wastewater: A review, J. Environ. Chem. Eng. 11 (2023) 109418, https://doi.org/10.1016/j.jece.2023.109418.

[14] J. Theerthagiri, J. Park, H.T. Das, N. Rahamathulla, E.S.F. Cardoso, A.P. Murthy, G. Maia, D.V.N. Vo, M.Y. Choi, Electrocatalytic conversion of nitrate waste into ammonia: a review, Environ. Chem. Lett 20 (2022) 2929–2949, https://doi.org/10.1007/s10311-022-01469-y.

[15] I. Katsounaros, On the assessment of electrocatalysts for nitrate reduction, Curr. Opinion Electrochem. 28 (2021) 100721, https://doi.org/10.1016/j.coelec.2021.100721.

[16] R. Oriol, E. Brillas, P.L. Cabot, J.L. Cortina, I. Sirés, Paired electrochemical removal of nitrate and terbuthylazine pesticide from groundwater using mesh electrodes, Electrochim. Acta 383 (2021) 138354, https://doi.org/10.1016/j.electacta.2021.138354.

[17] R. Oriol, M.P. Bernícola, E. Brillas, P.L. Cabot, I. Sirés, Paired electro-oxidation of insecticide imidacloprid and electrodenitrification in simulated and real water matrices, Electrochim. Acta 317 (2019) 753–765, https://doi.org/10.1016/j.electacta.2019.05.002.

[18] J. Ding, W. Li, Q.L. Zhao, K. Wang, Z. Zheng, Y.Z. Gao, Electroreduction of nitrate in water: Role of cathode and cell configuration, Chem. Eng. J. 271 (2015) 252–259, https://doi.org/10.1016/j.cej.2015.03.001.

[19] Z. Liu, C. Wang, C. Chen, C. Li, C. Guo, Selective electroreduction of nitrate to ammonia with high Faradaic efficiency on nanocrystalline silver, Electrochem. Commun. 131 (2021) 107121, https://doi.org/10.1016/j.elecom.2021.107121.

[20] X. Zhang, Y. Wang, C. Liu, Y. Yu, S. Lu, B. Zhang, Recent advances in non-noble metal electrocatalysts for nitrate reduction, Chem. Eng. J. 403 (2021) 126269, https://doi.org/10.1016/j.cej.2020.126269.

[21] J. Sun, S. Garg, J. Xie, C. Zhang, T.D. Waite, Electrochemical reduction of nitrate with simultaneous ammonia recovery using a flow cathode reactor, Environ. Sci. Technol. 56 (2022) 17298–17309, https://doi.org/10.1021/acs.est.2c06033.

[22] O.M. Cornejo, M.F. Murrieta, L.F. Castañeda, J.L. Nava, Characterization of the reaction environment in flow reactors fitted with BDD electrodes for use in electrochemical advanced oxidation processes: A critical review, Electrochim. Acta 331 (2020) 135373, https://doi.org/10.1016/j.electacta.2019.135373.

[23] F.F. Rivera, T. Pérez, L.F. Castañeda, J.L. Nava, Mathematical modeling and simulation of electrochemical reactors: A critical review, Chem. Eng. Sci. 239 (2021) 116622, https://doi.org/10.1016/j.ces.2021.116622.

[24] O. González Pérez, J.M. Bisang, Removal of nitrate using an activated rotating cylinder electrode, Electrochim. Acta 194 (2016) 448–453, https://doi.org/10.1016/j.electacta.2016.02.114.

[25] R. Oriol, J.L. Nava, E. Brillas, I. Sirés, Diffusion-charge transfer characterization of a rotating cylinder electrode reactor used for the complete electrocatalytic removal of nitrate from water, J. Environ. Chem. Eng. 10 (2022) 108839, https://doi.org/10.1016/j.jece.2022.108839.

[26] J.R. Hernández-Tapia, J. Vazquez-Arenas, I. González, Electrochemical reactor with rotating cylinder electrode for optimum electrochemical recovery of nickel from plating rinsing effluents, J. Hazard. Mater. 262 (2013) 709–716, https://doi.org/10.1016/j.jhazmat.2013.09.029.

[27] J.L. Arredondo, F.F. Rivera, J.L. Nava, Silver recovery from an effluent generated by plating industry using a rotating cylinder electrode (RCE), Electrochim. Acta 147 (2014) 337–342, https://doi.org/10.1016/j.electacta.2014.09.127.

[28] J.A. Barragan, M. Tesillo-Perales, J.R. Alemán-Castro, E.R. Larios-Durán, E. P. Rivero, Optimization of a rotating cylinder electrode electrochemical reactor for metal recovery: An innovative approach and method combining CFD and response surface methodology, Electrochim. Acta 435 (2022) 141335, https://doi.org/10.1016/j.electacta.2022.141335.

[29] O.M. Cornejo, I. Sirés, J.L. Nava, Cathodic generation of hydrogen peroxide sustained by electrolytic O_2 in a rotating cylinder electrode (RCE) reactor, Electrochim. Acta 404 (2022) 139621, https://doi.org/10.1016/j.electacta.2021.139621.

[30] A.H. Abbar, R.H. Salman, A.S. Abbas, Studies of mass transfer at a spiral-wound woven wire mesh rotating cylinder electrode, Chem. Eng. Process.: Process Intensif. 127 (2018) 10–16, https://doi.org/10.1016/j.cep.2018.03.013.

[31] F. Walsh, A First Course in Electrochemical Engineering, first ed., The Electrochemical Consultancy, Romsey, 1993.

[32] E.P. Rivero, M.R. Cruz-Díaz, F.J. Almazán-Ruiz, I. González, Modeling the effect of non-ideal flow pattern on tertiary current distribution in a filter-press-type electrochemical reactor for copper recovery, Chem. Eng. Res. Des. 100 (2015) 422–433, https://doi.org/10.1016/j.cherd.2015.04.036.

[33] J. Valentín-Reyes, J.L. Nava, Modeling of a novel cascade-type electrocoagulation reactor using iron electrodes. Characterization of bubbling flow and coagulant dosage, Chem. Eng. Process.: Process Intensif. 189 (2023) 109411, https://doi.org/10.1016/j.cep.2023.109411.

[34] M.F. Murrieta, J.L. Nava, Electrosynthesis of hypochlorous acid in a filter-press electrolyzer and its modeling in dilute chloride solutions, J. Electroanal. Chem. 892 (2021) 115286, https://doi.org/10.1016/j.jelechem.2021.115286.

[35] A.D. Villalobos-Lara, T. Pérez, A.R. Uribe, J.A. Alfaro-Ayala, J.J. Ramírez-Minguela, J.I. Minchaca-Mojica, CFD simulation of biphasic flow, mass transport and current distribution in a continuous rotating cylinder electrode reactor for electrocoagulation process, J. Electroanal. Chem. 858 (2020) 113807, https://doi.org/10.1016/j.jelechem.2019.113807.

[36] E.P. Rivero, P. Granados, F.F. Rivera, M. Cruz, I. González, Mass transfer modeling and simulation at a rotating cylinder electrode (RCE) reactor under turbulent flow for copper recovery, Chem. Eng. Sci. 65 (2010) 3042–3049, https://doi.org/10.1016/j.ces.2010.01.030.

[37] L. Castañeda, R. Antaño, F.F. Rivera, J.L. Nava, Computational fluid dynamic simulations on single-phase flow in a spacer-filled channel of a filter-press electrolyzer, Int. J. Electrochem. Sci. 12 (2017) 7351–7364. https://doi.org/10.20964/2017.08.09.

[38] F.F. Rivera, L.C. Castañeda, P.E. Hidalgo, G. Orozco, Study of hydrodynamics at Asahi^{TM} prototype electrochemical flow reactor, using computational fluid dynamics and experimental characterization techniques, Electrochim. Acta 245 (2017) 107–117, https://doi.org/10.1016/j.electacta.2017.05.134.

[39] M.R. Cruz-Díaz, E.P. Rivero, F.J. Almazán-Ruiz, Á. Torres-Mendoza, I. González, Design of a new FM01-LC reactor in parallel plate configuration using numerical simulation and experimental validation with residence time distribution (RTD), Chem. Eng. Process.: Process Intensif. 85 (2014) 145–154, https://doi.org/10.1016/j.cep.2014.07.010.

[40] A. Rodríguez, F.F. Rivera, G. Orozco, G. Carreño, F. Castañeda, Analysis of inlet and gap effect in hydrodynamics and mass transport performance of a multipurpose electrochemical reactor: CFD simulation and experimental validation, Electrochim. Acta 282 (2018) 520–532, https://doi.org/10.1016/j.electacta.2018.06.071.

[41] J.A. Barrios, F.E. Solís-Caballero, A. Cano, U. Durán, G. Orozco, F.F. Rivera, Two-phase hydrodynamic modelling and experimental characterization in an activated sludge electrooxidation flow reactor, Chem. Eng. Res. Des. 141 (2019) 339–349, https://doi.org/10.1016/j.cherd.2018.11.005.

[42] M.A. Sandoval, R. Fuentes, F.C. Walsh, J.L. Nava, Computational fluid dynamics simulations of single-phase flow in a filter-press flow reactor having a stack of three

cells, Electrochim. Acta 216 (2016) 490–498, https://doi.org/10.1016/j.electacta.2016.09.045.

[43] O.M. Cornejo, J. Valentín-Reyes, M. Rosales, J.L. Nava, Simulations of aluminum dosage and H_2O–H_2 flow in a pre-pilot twelve-cell electrocoagulation stack, Chem. Eng. J. 450 (2022) 138222, https://doi.org/10.1016/j.cej.2022.138222.

[44] M. Rosales, J.L. Nava, Simulations of turbulent flow, mass transport, and tertiary current distribution on the cathode of a rotating cylinder electrode reactor in continuous operation mode during silver deposition, J. Electrochem. Soc. 164 (2017) E3345–E3353. https://iopscience.iop.org/article/10.1149/2.0351711jes.

[45] A.N. Colli, J.M. Bisang, Time-dependent mass-transfer behaviour under laminar and turbulent flow conditions in rotating electrodes: A CFD study with analytical and experimental validation, Int. J. Heat Mass Transf. 137 (2019) 835–846, https://doi.org/10.1016/j.ijheatmasstransfer.2019.03.152.

[46] E.P. Rivero, F.A. Rodríguez, M.R. Cruz-Díaz, I. González, Reactive diffusion migration layer and mass transfer wall function to model active chlorine generation in a filter press type electrochemical reactor for organic pollutant degradation, Chem. Eng. Res. Des. 138 (2018) 533–545, https://doi.org/10.1016/j.cherd.2018.07.010.

[47] S.T. McBeath, A. Nouri-Khorasani, M. Mohseni, D.P. Wilkinson, In-situ determination of current density distribution and fluid modeling of an electrocoagulation process and its effects on natural organic matter removal for drinking water treatment, Water Res. 171 (2020) 115404, https://doi.org/10.1016/j.watres.2019.115404.

[48] T. Pérez, L.F. Arenas, D. Villalobos-Lara, N. Zhou, S. Wang, F.C. Walsh, J.L. Nava, C. Ponce de León, Simulations of fluid flow, mass transport and current distribution in a parallel plate flow cell during nickel electrodeposition, J. Electroanal. Chem. 873 (2020) 114359, https://doi.org/10.1016/j.jelechem.2020.114359.

[49] H.K Versteeg, W. Malalasekera, An Introduction to Computational Fluid Dynamics: The Finite Volume Method, Second ed., Prentice Hall, London, 1995.

[50] B.E. Launder, D.B. Spalding, The numerical computation of turbulent flow, Comput. Methods Appl. Mech. Eng. 3 (1974) 269–289, https://doi.org/10.1016/0045-7825(74)90029-2.

[51] A.D. Villalobos-Lara, B. Castillo, F.F. Rivera, J. Vázquez-Arenas, Model accounting for the Cr(III) electroprecipitation kinetics in an electrochemical reactor based on CFD and mass transport contributions, J. Electroanal. Chem. 928 (2023) 117057, https://doi.org/10.1016/j.jelechem.2022.117057.

[52] C. Zhang, Y. Liu, W. Jiao, G. Qi, J. Guo, A turbulent mass diffusivity model for the simulation of the biodegradation of toluene in an internal loop airlift reactor, Process Saf. Environ. Prot. 165 (2022) 646–657, https://doi.org/10.1016/j.psep.2022.07.042.

[53] T. Pérez, J.L. Nava, Numerical simulation of the primary, secondary and tertiary current distributions on the cathode of a rotating cylinder electrode cell. Influence of using plates and a concentric cylinder as counter electrodes, J. Electroanal. Chem. 719 (2014) 106–112, https://doi.org/10.1016/j.jelechem.2014.02.010.